Smart Materials and Structures

Numerical modelling of micro energy harvesting systems based on piezoelectric composites polarized with interdigitated electrodes

To cite this article before publication: Ahmad Eduardo Guennam *et al* 2020 *Smart Mater. Struct.* in press https://doi.org/10.1088/1361-665X/ab87e2

Numerical Modelling of Micro Energy Harvesting Systems based on Piezoelectric Composites Polarized with Interdigitated Electrodes

Ahmad E. Guennam[1], Bibiana M. Luccioni[2,3]

[1] Departamento de Ciencias de la Computación, Universidad Nacional de Tucumán. Avenida Independencia 1800, SM de Tucuman, Argentina
[2] Instituto de Estructuras, Universidad Nacional de Tucumán. Avenida Independencia 1800, SM de Tucuman, Argentina
[3] CONICET, Av Rivadavia 1917, CABA, Argentina

E-mail: eguennam@herrera.unt.edu.ar

Abstract. This paper focuses on the numerical modelling of micro-energy harvesting systems(MEHSs) based on piezoelectric composites polarised with interdigitated electrodes (PCPIE). The system response and the harvested energy are numerically assessed using a multilayer piezoelectric shell finite element (FE) with a uniform fibre aligned electric field (UFAEF) in each active layer. Circuit and compatibility equations are included to take into account the presence of the electrical network. A state-space (SS) model is derived and used to evaluate the effect of electrical impedance on damping and natural frequencies, as well as dissipated energy/power. An energy harvester beam with a piezoelectric macro fibre composite (MFC) patch is first modelled with the developed tools. Numerical results are found to be in good agreement with experimental results reported in the literature. Finally, a MEHS consisting of a closed-box beam equipped with PCPIE devices bonded to its skin is analysed. The structural system is subjected to dynamic loading imposing oscillating displacements and deformations compatibles with those expected during service-life. Numerical results show the influence of the electrical impedance on system response, damping, natural frequencies, and electrical power.

Keywords: Piezoelectric, Composites, Energy Harvesting, Shell FE

Submitted to: *Smart Mater. Struct.*

1. Introduction

Wireless sensing devices usage is continuously growing nowadays. Computer mouses, play console joysticks, smartphones, smart tires, helicopter blades monitoring systems and remote sensing stations to name a very few, can be found in daily life. The applications mentioned above are typically powered by batteries having to be periodically replaced or recharged. An energy harvesting (EH) system powering those applications could be highly advantageous.

Advances observed in electronics, circuitry miniaturization and the decrease in devices power consumption made EH an attractive option to power microelectronics. The possibility of installing sensor stations without the need for replacing batteries and lightening maintenance needs is an advantage clearly identified in the scientific literature. MEHS are potentially useful as energy suppliers for remote electronic systems or those of difficult access for batteries replacement.

A bibliographical survey reflects that this is a subject of growing scientific and technological interest. Sensors applications in helicopters [1], biomedicine [2, 3], wearable electronics for health monitoring [4, 5], tactile sensors [6], animal tracking systems [7], bridge and tall tower monitoring stations [8], pneumatic tires [9, 10], wind turbine and fan blades, deep submerged and oil drilling systems [11], and piezoelectric floors [12] are of main relevance. Active structural systems, miniaturized electronics, and wireless communication are successfully combined to build up self-powered systems with diverse functionality. Those systems have a common feature: they are equipped with some variant of EH system.

One popular kind of energy harvesting system is based on piezoelectric materials. In particular, piezoelectric composites polarized with Interdigitated electrodes (IE) pattern allows achieving high electromechanical coupling, maintaining essential composite material features such as high anisotropy and conformability to complex shapes.

Several authors have investigated the damping produced by energy dissipation in a passive electrical network connected to the electrodes of piezoelectric devices. Hagood and Flotow [13] analysed the effect of connecting a shunting resistive and inductive circuit to piezoelectric devices bonded to a cantilever beam. They observed that the effect was similar to that produced when adding a viscoelastic material. Later, other authors considered electrical networks connected to beams, plates and shells. Koshigoe and Murdock [14] studied active and passive damping produced in plates with piezoelectric transducers. Saravanos [15] analysed the damping produced in laminated plates depending on the resistive level. Lesieutre *et al.* [16] studied the damping produced by EH on electronic circuits connected to a two-layer bimorph. Aridogan *et al.* [17] worked with thin plate structures for EH from stationary random vibrations. Moreover, a variety of piezoelectric materials and configurations have been proposed and analysed. Xu *et al.* [18] investigated EH issues in systems using multilayer piezoelectric stacks combined with supercapacitors; they proposed theoretical models and performed experimental validations. Ramadan *et al.* [6] presented a review of bulk piezopolymers,

piezo composites and voided charged polymers regarding electromechanical properties and their applications. They emphasize the advantage of using piezoelectric composites in EH applications due to their high coupling coefficients.

Suitable structure predictive tools are of primary importance when designing and assessing MEHS. In the last 30 years, a great effort has been made in the field of piezoelectric materials and structure modelling. Scientists and engineers have proposed a wide variety of approaches and models for the analysis of piezoelectric systems using numerical methods. In particular, the finite element method (FEM) has received outstanding attention. Almost twenty years ago, Benjeddou [19] presented a survey of trends and advances in formulations and applications of finite elements related to piezoelectric materials and structural systems. Since then, the field has remarkably grown, evidencing its scientific interest and technological importance. A bibliography survey reflects active research in several branches [20, 21, 22] showing that the modelling of piezoelectric composite based EH systems is an expanding research field.

A key aspect of PCPIE is that the electric field (EF) inside the fibres is not uniform, especially near electrode fingers. Nevertheless, far enough from electrodes, EF can be considered uniform and running almost parallel to the fibres. When the modelling purpose is the description of macroscopic behaviour, homogenization strategies are successfully employed to obtain the composite properties. A useful modelling strategy for thin smart structures consists of combining a homogenization material model for the piezoelectric composite (HMMPC) with suitable plate, shell or membrane finite elements. In a piezoelectric material region covered by the same electrodes, a constant homogenized electric field (HEF) is a valid assumption since electrodes are electrical equipotential regions. Therefore, FE models with the ability of efficiently introducing a constant EF through the volume covered by the same electrode pair are worthy. If a PCPIE region is discretized using elements with the same nodes for both geometry and electric potential DOFs, the electric field and geometry will be coupled. Arbitrary shapes and unstructured meshes may require suitable constraints between electric DOFs to enforce a constant electric field over the FE assemblage. In this context, a uniform fibre aligned electric field (UFAEF) linked to the electric potential of an exclusively electric node seems to be more suitable. The main objective of this approach is to decouple the electric field from the element geometry using different nodes for the mechanical and electrical DOFs.

The piezoelectric multilaminate shell formulation proposed in [23] uses the UFAEF concept, allowing the electric field on each active layer to be easily introduced in desired directions, typically parallel to the fibres, and with its magnitude dependent on the electric potential value and electrode spacing.

The performance of EH systems is strongly influenced by the geometry of the structure. Pradeesh and Udhayakumar [24], and Paquin and St-Amant [25] studied the effects of beam geometry and thickness on energy harvested with mounted piezoelectric materials. The FE shell with UFAEF described in this paper can substantially simplify the modelling of irregular shapes and variable thickness structures equipped with

piezoelectric composite materials.
This paper focuses on the numerical modelling of MEHSs based on PCPIE. The specially formulated piezoelectric shell FE with UFAEF is implemented along with electrical circuit and compatibility equations included to take into account the electrical impedance. A whole modelling and simulation package named PEMPack was fully developed and implemented by the authors in GNU/Octave V5.0.2 [26]. The developed package binds an FE module, an electrical circuit module, a system solver module and a post-processing toolset.

An EH system experimentally studied by Upadrashta and Yang [27] is first analysed and numerical and experimental results are compared to validate the proposed model. Then, numerical experiments are successfully conducted with the developed package highlighting the capability of the proposed tool to capture the influence of the electrical impedance on system response, damping, natural frequencies and electrical power output.

2. System Modelling

Energy harvesting systems considered in this paper are composed of two coupled subsystems, namely, a piezoelectric structure and a passive electrical network. Both subsystems are modelled and the equations describing their behaviour are coupled and solved.

2.1. Piezoelectric Structural model

All the development and analysis conducted in this work rely on the assumptions of geometrical and material linear behaviour. The former hypothesis is valid for low displacement and strains levels. Regarding the latter, as long as voltage levels remain moderate, no repolarisation is expected and linear or quasi-linear (linearized) electromechanical elastic material behaviour can be assumed.

A piezoelectric structural subsystem consisting of a thin-walled structure with piezo composite laminates bonded to its skin is considered in this paper. The structure equation of motion is derived based on an FE model using the piezoelectric shell FE proposed in [23].

As mentioned in the preceding section, standard shell and plate piezoelectric finite elements interpolate the electric potential inside the element based on values at nodes located to correctly represent the geometry. Then, the electric field is calculated as the electric potential gradient. When modelling PCPIE using UFAEF assumption, a nodal electric potential distribution has to be imposed such that the resulting electric field calculated as the gradient of the interpolated electric potential gives rise to the target UFAEF. For example, a quite simple squared piezoelectric patch discretized with regular $n \times n$ elements as shown in figure 1(a) requires extra calculations for the voltage distribution in order to effectively achieve a uniform electric field.

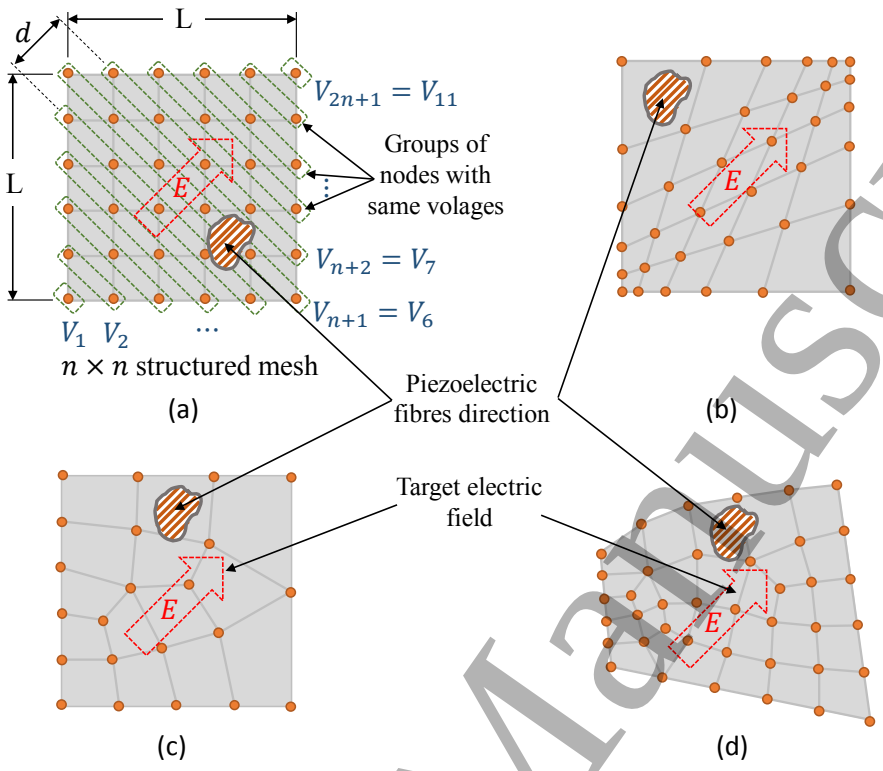

Figure 1. (a) Simple geometry/structured mesh. (b) Simple geometry/structured, distorted mesh. (c) Regular geometry/unstructured mesh. (d) Non-regular geometry/ unstructured mesh

For the simple geometry and mesh shown in figure 1(a), the electric potential required on each node group to impose electric field oriented as indicated is calculated according to

$$V_i = E\sqrt{2}L\left(1 - \frac{1-i}{2n}\right) \tag{1}$$

where V_i is the electric potential imposed on node group i, L is the side length, n is the number of elements per side and E is the desired electric field. These calculations could be quite complicated for distorded or unstructured meshes as those shown in figures 1(b) and (c), or for non-regular shapes as that depicted in figure 1(d). If classical formulations are used, nodal electric potential value distributions that guarantee the target electric field direction are not trivial in these cases.

To tackle this pitfall, the piezoelectric shell FE with UFAEF [23], specially formulated for piezoelectric composites with interdigitated electrodes, is used to model the active structure zones. Figure 2 schematically shows the shell FE with UFAEF.

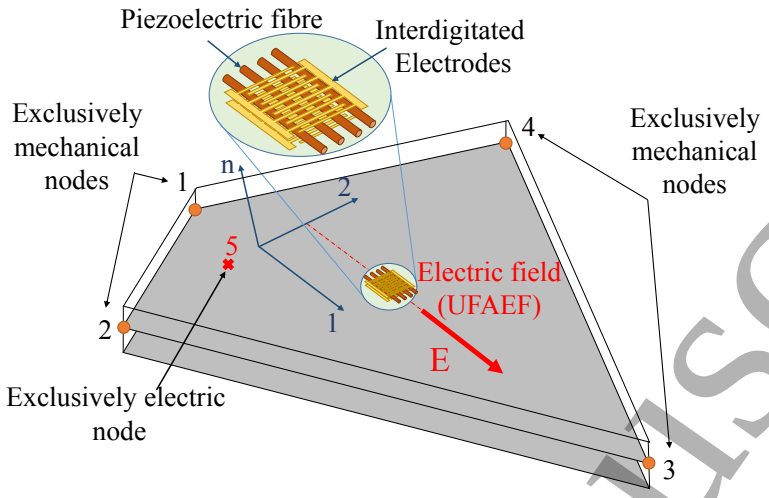

Figure 2. Piezoelectric shell FE with UFAEF.

Figure 3 shows a structure with PCPIE active zone and the FE mesh with exclusively electrical and mechanical nodes.

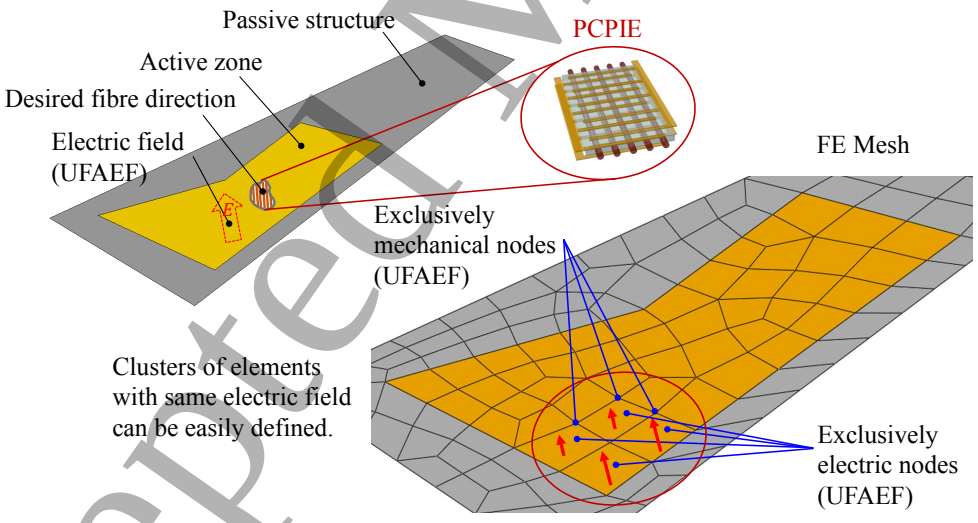

Figure 3. Non-regular mesh with target electric field running parallel to fibres.

The UFAEF description, in conjunction with an HMMPC, is an attractive modelling tool. The proposed tool allows the analysis of active structures not only using an affordable number of degrees of freedoms but also having a positive trade-off between result quality, model building time and solver-runtime.

In each piezoelectric layer, the electric node potential and electrode separation determine the magnitude of the electric field, while the fibres orientation settles its direction.

The electromechanical FE equation of motion reads

$$\left\{ \begin{array}{c} \mathbf{F}_m \\ \mathbf{F}_e \end{array} \right\} = \left[\begin{array}{cc} \mathbf{M}_{mm} & \mathbf{0} \\ \mathbf{0} & \mathbf{0} \end{array} \right] \left\{ \begin{array}{c} \ddot{\mathbf{d}}_m \\ \ddot{\mathbf{d}}_e \end{array} \right\} + \left[\begin{array}{cc} \mathbf{C}_{mm} & \mathbf{0} \\ \mathbf{0} & \mathbf{0} \end{array} \right] \left\{ \begin{array}{c} \dot{\mathbf{d}}_m \\ \dot{\mathbf{d}}_e \end{array} \right\} + \left[\begin{array}{cc} \mathbf{K}_{mm} & \mathbf{K}_{me} \\ \mathbf{K}_{em} & \mathbf{K}_{ee} \end{array} \right] \left\{ \begin{array}{c} \mathbf{d}_m \\ \mathbf{d}_e \end{array} \right\} \tag{2}$$

Equation (2) embosses the presence of mechanical and electrical degrees of freedom, $\mathbf{d}_m$ and $\mathbf{d}_e$, respectively. $\ddot{\mathbf{d}}_m$ is the acceleration vector, while $\dot{\mathbf{d}}_m$ is the velocity vector, $\mathbf{F}_m$ and $\mathbf{F}_e$ are consistent nodal mechanical force and electric charge vectors, respectively. $\mathbf{K}_{mm}$, $\mathbf{K}_{me}$ and $\mathbf{K}_{ee}$ are mechanical stiffness, piezoelectric coupling and dielectric matrices, respectivelly. Besides, $\mathbf{M}_{mm}$ and $\mathbf{C}_{mm}$ are mass and damping matrices, respectively.

After assembling the FE matrices and vectors, a convenient partitioning is performed in order to separate the mechanical (m) and electrical (e) DOFs. Some DOFs have prescribed values while the rest are left free. Thus, a second partitioning is performed in order to separate prescribed (p) DOFs from free (f) DOFs. After both partitionings, the system reads

$$\begin{aligned} \left\{ \begin{array}{c} \mathbf{F}_m^f \\ \mathbf{F}_e^f \\ \mathbf{F}_m^p \\ \mathbf{F}_e^p \end{array} \right\} = & \left[\begin{array}{cccc} \mathbf{M}_{mm}^{ff} & \mathbf{0} & \mathbf{M}_{mm}^{fp} & \mathbf{0} \\ \mathbf{0} & \mathbf{0} & \mathbf{0} & \mathbf{0} \\ \mathbf{M}_{mm}^{pf} & \mathbf{0} & \mathbf{M}_{mm}^{pp} & \mathbf{0} \\ \mathbf{0} & \mathbf{0} & \mathbf{0} & \mathbf{0} \end{array} \right] \left\{ \begin{array}{c} \ddot{\mathbf{d}}_m^f \\ \ddot{\mathbf{d}}_e^f \\ \ddot{\mathbf{d}}_m^p \\ \ddot{\mathbf{d}}_e^p \end{array} \right\} \\ & + \left[\begin{array}{cccc} \mathbf{C}_{mm}^{ff} & \mathbf{0} & \mathbf{C}_{mm}^{fp} & \mathbf{0} \\ \mathbf{0} & \mathbf{0} & \mathbf{0} & \mathbf{0} \\ \mathbf{C}_{mm}^{pf} & \mathbf{0} & \mathbf{C}_{mm}^{pp} & \mathbf{0} \\ \mathbf{0} & \mathbf{0} & \mathbf{0} & \mathbf{0} \end{array} \right] \left\{ \begin{array}{c} \dot{\mathbf{d}}_m^f \\ \dot{\mathbf{d}}_e^f \\ \dot{\mathbf{d}}_m^p \\ \dot{\mathbf{d}}_e^p \end{array} \right\} \\ & + \left[\begin{array}{cccc} \mathbf{K}_{mm}^{ff} & \mathbf{K}_{me}^{ff} & \mathbf{K}_{mm}^{fp} & \mathbf{K}_{me}^{fp} \\ \mathbf{K}_{em}^{ff} & \mathbf{K}_{ee}^{ff} & \mathbf{K}_{em}^{fp} & \mathbf{K}_{ee}^{fp} \\ \mathbf{K}_{mm}^{pf} & \mathbf{K}_{me}^{pf} & \mathbf{K}_{mm}^{pp} & \mathbf{K}_{me}^{pp} \\ \mathbf{K}_{em}^{pf} & \mathbf{K}_{ee}^{pf} & \mathbf{K}_{em}^{pp} & \mathbf{K}_{ee}^{pp} \end{array} \right] \left\{ \begin{array}{c} \mathbf{d}_m^f \\ \mathbf{d}_e^f \\ \mathbf{d}_m^p \\ \mathbf{d}_e^p \end{array} \right\} \end{aligned} \tag{3}$$

Writing down the first two rows of equation (3) and regrouping some terms, the following equations for free mechanical and electric DOFs are obtained:

$$\mathbf{M}_{mm}^{ff}\ddot{\mathbf{d}}_m^f + \mathbf{C}_{mm}^{ff}\dot{\mathbf{d}}_m^f + \mathbf{K}_{mm}^{ff}\mathbf{d}_m^f + \mathbf{K}_{me}^{ff}\mathbf{d}_e^f = \hat{\mathbf{F}}_m^f \tag{4}$$

$$\mathbf{K}_{em}^{ff}\mathbf{d}_m^f + \mathbf{K}_{ee}^{ff}\mathbf{d}_e^f = \hat{\mathbf{F}}_e^f \tag{5}$$

The right hand sides in Eqs (4) and (5),

$$\hat{\mathbf{F}}_m^f = \mathbf{F}_m^f - \mathbf{M}_{mm}^{fp}\ddot{\mathbf{d}}_m^p - \mathbf{C}_{mm}^{fp}\dot{\mathbf{d}}_m^p - \mathbf{K}_{mm}^{fp}\mathbf{d}_m^p - \mathbf{K}_{me}^{fp}\mathbf{d}_e^p \tag{6}$$

and

$$\hat{\mathbf{F}}_e^f = \mathbf{F}_e^f - \mathbf{K}_{em}^{fp}\mathbf{d}_m^p - \mathbf{K}_{ee}^{fp}\mathbf{d}_e^p \tag{7}$$

are, respectively, the modified mechanical and electrical nodal forces applied to free DOFs. Both, equation (6) and equation (7) have contributions from prescribed DOFs, being electric potentials, accelerations and displacements. Note that all upperscripts on the left hand side of equations (4) and (5) are f and ff meaning *free*. These equations describe the evolution of free DOFs. For them, the notation can be notablly simplified as follows:

$$\mathbf{M}\ddot{\mathbf{u}} + \mathbf{C}_d\dot{\mathbf{u}} + \mathbf{K}\mathbf{u} + \mathbf{K}_{piezo}\mathbf{V} = \mathbf{F} \tag{8}$$

$$\mathbf{K}_{piezo}^T\mathbf{u} + \mathbf{K}_{diel}\mathbf{V} = \mathbf{Q} \tag{9}$$

where:

$$\begin{aligned}
\mathbf{M} &= \mathbf{M}_{mm}^{ff}, \\
\mathbf{C}_d &= \mathbf{C}_{mm}^{ff}, \\
\mathbf{K} &= \mathbf{K}_{mm}^{ff}, \\
\mathbf{K}_{piezo} &= \mathbf{K}_{me}^{ff}, \\
\mathbf{K}_{diel} &= \mathbf{K}_{ee}^{ff}, \\
\mathbf{u} &= \mathbf{d}_m^f, \\
\mathbf{V} &= \mathbf{d}_e^f, \\
\mathbf{F} &= \hat{\mathbf{F}}_m^f, \\
\mathbf{Q} &= \hat{\mathbf{F}}_e^f
\end{aligned} \tag{10}$$

A global form of damping is considered in this paper. Following Clough and Penzien [28] the damping matrix is calculated based on a given set of modal damping ratios as,

$$\mathbf{C_d} = \mathbf{M}\left[\sum_{n=1}^{N}\frac{2\zeta_n\omega_n}{M_n}\Phi_n\Phi_n^T\right]\mathbf{M} \tag{11}$$

where M_n Φ_n, ω_n and ζ_n are the mass matrix, modal shapes, modal fequency and modal damping ratio, respectively.

It is interesting to distinguish between two conditions, namely, open-circuit (OC) and short-circuit (SC). In open-circuit condition there are some electric degrees of freedom that are not restrained ($\mathbf{d}_e^f$). Clearing V from equation 9 and replacing it in equation 8, the following equation is obtained

$$\mathbf{M}\ddot{\mathbf{u}} + \mathbf{C}_d\dot{\mathbf{u}} + (\mathbf{K} - \mathbf{K}_{piezo}\mathbf{K}_{diel}^{-1}\mathbf{K}_{piezo}^T)\mathbf{u} = \mathbf{F} - \mathbf{K}_{piezo}\mathbf{K}_{diel}^{-1}\mathbf{Q} \tag{12}$$

In short-circuit condition $V = 0$ and equation 8 reduces to

$$\mathbf{M}\ddot{\mathbf{u}} + \mathbf{C}_d\dot{\mathbf{u}} + \mathbf{K}\mathbf{u} = \mathbf{F} \tag{13}$$

An eigenvalue analysis could be performed for both, OC and SC conditions and the corresponding natural frequencies can be extracted. Modified stiffness matrix

$\mathbf{K}^* = \mathbf{K} - \mathbf{K}_{piezo}\mathbf{K}_{diel}^{-1}\mathbf{K}_{piezo}^T$ is used in the former condition, while $\mathbf{K}^* = \mathbf{K}$ is used in the later, when the generalized eigenvalue problem is stated.

At this point, the structural system model has been stated. From the EH point of view this model is quite general since it admits the presence of both mechanical and electrical, restrained and free DOFs. The electrical, restrined DOFs are a subgroup where electric potential could be directly imposed. As shown in equations (6) and (7), the mechanical $\mathbf{K}_{me}^{fp}\mathbf{d}_e^p$ and elecectrical $\mathbf{K}_{ee}^{fp}\mathbf{d}_e^p$ terms represent contributions of prescribed electric potentials to the right-hand-side (RHS) of equations (8) and (9). The electrical free DOFs can be used as sensor or energy extraction ports as well. The evolution of the voltage on the electric free DOFs will be influenced by the characteristics and behaviour of the circuit connected to it. This issue is detailled in the next section.

2.2. Passive Electrical Network modelling

Circuit equations based on Kirchhoff's law are included and coupled to the structural model equations using compatibility conditions of electric variables on connection nodes. An extended equation system including the electrical circuit is obtained.
When the electrical circuit is connected to a voltage source, the electric current, voltages, and energy are mathematically described using Kirchhoff's law and electric charge conservation principle. The electrical network complexity can range from a single resistance to a sophisticated circuit. The present work aims to quantify the electrical energy extracted without going into details about the electrical circuit. A wide variety of electrical circuits could be analysed using simple combinations of equivalent resistive, inductive and capacitive characteristics.

The circuit equations are coupled with the structural, electromechanical equations (equations (8) and (9)) using electric compatibility conditions, namely, the voltage across piezoelectric electrodes and the time derivative of the electric charge flowing through them should be coincident with those feeding the circuit.

The general case of a Resistive-Inductive-Capacitive (RLC) circuit is first considered in this paper. Afterwards, particular cases such as resistive-inductive (RL), resistive-capacitive (RC) and pure capacitive (C) circuit are addressed. In each case, the time domain circuit equations are presented and recast to be coupled to equations (8) and (9).

3. State Space Model

The structure equations of motion are recast into SS form and circuit equations are included to obtain a numerical predictive tool allowing whole system evaluation performance under main parameter variations. SS approach is a useful tool to represent the EH system and to solve the equations of motion in both time and frequency domains.

The SS system representation is expressed as follows:

$$\begin{aligned} \dot{\mathbf{x}}(\mathbf{t}) &= [\mathbf{A}]\mathbf{x}(\mathbf{t}) + [\mathbf{B}]\mathbf{q}(\mathbf{t}) \\ \mathbf{y}(\mathbf{t}) &= [\mathbf{D_1}]\mathbf{x}(\mathbf{t}) + [\mathbf{D_2}]\mathbf{q}(\mathbf{t}) \end{aligned} \tag{14}$$

where $\mathbf{x}(\mathbf{t})$ is the state vector, $\mathbf{q}(\mathbf{t})$ is the input vector and $\mathbf{y}(\mathbf{t})$ is the output vector. Besides, $[\mathbf{A}]$ and $[\mathbf{B}]$ are system and input matrices respectivelly while $[\mathbf{D_1}]$ and $[\mathbf{D_2}]$ are output matrices.

In order to obtain the SS model of a piezoelectric structure coupled with an electrical circuit, the classical variables representing the energy in the structural system and those describing the energy stored in the inductor and the capacitor are first identified. The energy stored in the inductor is proportional to the current $J = \frac{\partial \mathbf{Q}}{\partial t}$ while the energy stored in the capacitor is defined by the voltage V_c.

Equation(14) can be conveniently recasted to bring the input vector $\mathbf{q}(\mathbf{t})$ on the right-hand side,

$$\begin{aligned} [\mathbf{A}^*]\dot{\mathbf{x}}(\mathbf{t}) + [\mathbf{B}^*]\mathbf{x}(\mathbf{t}) &= \mathbf{q}(\mathbf{t}) \\ [\mathbf{D_1^*}]\mathbf{y}(\mathbf{t}) + [\mathbf{D_2^*}]\mathbf{x}(\mathbf{t}) &= \mathbf{q}(\mathbf{t}) \end{aligned} \tag{15}$$

Using simple algebra manipulation,

$$\begin{aligned} [\mathbf{A}] &= -[\mathbf{A}^*]^{-1}[\mathbf{B}^*] \\ [\mathbf{B}] &= [\mathbf{A}^*]^{-1} \end{aligned} \tag{16}$$

Combining equations of motion with suitable circuit equations and defining the state vector according to the circuit layout, SS models are obtained for each case. In what follows, different circuit layouts are considered and coupled system state-space models are obtained.

The linear behaviour hypothesis allows to efficiently recast the model equations in the SS and to perform a large number of useful calculations in a relatively simple way. However, when nonlinear (material, geometric, loading, circuit) behaviour is expected, the developed equations are no longer strictly valid. In those cases, depending on the non-linearities, linearized equations could be considered to obtain SS models and a step-by-step time integration approach should be used.

Differential equations are stated for each electrical circuit layout and then inserted into system SS equations.

3.1. RLC-Series Circuit

An RLC series circuit connected to a piezoelectric source is depicted in figure 5 where J denotes the electric current, C is the capacitance, L is the inductance, and R is the electrical resistance. V_C, V_L and V_R are the voltage drop across each of them, respectivelly.

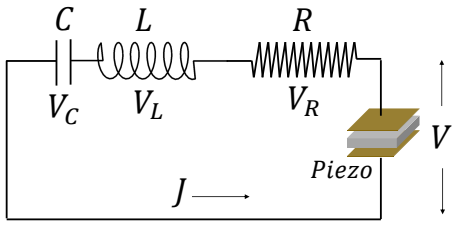

Figure 4. Scheme of a piezoelectric device connected to a RLC-Series circuit.

According to Kirchhoff's second law, the applied voltage equals the sum of voltage drops across the resistor, inductor and capacitor:

$$V = RJ + L\dot{J} + Q(t)/C \tag{17}$$

The electric current is defined as the time derivative of the electric charge, i.e. $J = \frac{\partial \mathbf{Q}}{\partial t}$. In RLC-Series circuit, J flowing through each component is the same than the current through the piezoelectric device. In this case, J is calculated as the time derivative of the electric charge Q arising in those electric DOFs left free and where the electrical circuit is connected, i.e. $J = \frac{\partial \hat{\mathbf{F}}_e^f}{\partial t} = \frac{\partial \mathbf{Q}}{\partial t}$.

Taking the time derivative of equation (17), it results:

$$\dot{V} = R\dot{J} + L\ddot{J} + \dot{V}_c \tag{18}$$

where $\dot{\mathbf{V}}_\mathbf{c} = \mathbf{C}^{-1}J$ is the voltage across the capacitor. To obtain the SS model, variables defining the energy stored in the structural system, inductor and capacitor, are identified. The energy stored in the inductor is quantified by the current J_L (for series connection $J_L = J_R = J$) while the energy stored in the capacitor is proportional to the voltage V_c across it.

The time derivative of equation (9) reads,

$$\mathbf{K}_{piezo}^T\dot{\mathbf{u}} + \mathbf{K}_{diel}\dot{\mathbf{V}} - \mathbf{R}^{-1}\mathbf{V} + \mathbf{R}^{-1}\mathbf{L}\dot{\mathbf{J}} = 0 \tag{19}$$

From equations (8), (19) and (18), taking into account the time derivative of the voltage across the capacitor, the following equation can be obtained,

$$\dot{\mathbf{V}}_\mathbf{c} - \mathbf{C}^{-1}J = 0 \tag{20}$$

Defining $\{\dot{\mathbf{u}}, \mathbf{u}, \mathbf{V}, \mathbf{J}, \mathbf{V_c}\}^T$ as the state vector, SS matrices are expressed as:

$$\begin{bmatrix} \mathbf{M} & \mathbf{0}_{a\times a} & \mathbf{0}_{a\times b} & \mathbf{0}_{a\times b} & \mathbf{0}_{a\times b} \\ \mathbf{0}_{a\times a} & \mathbf{I}_{a\times a} & \mathbf{0}_{a\times b} & \mathbf{0}_{a\times b} & \mathbf{0}_{a\times b} \\ \mathbf{0}_{b\times a} & \mathbf{0}_{b\times a} & \mathbf{K}_{diel} & \mathbf{0}_{b\times b} & \mathbf{0}_{b\times b} \\ \mathbf{0}_{b\times a} & \mathbf{0}_{b\times a} & \mathbf{0}_{b\times b} & \mathbf{I}_{b\times b} & \mathbf{0}_{b\times b} \\ \mathbf{0}_{b\times a} & \mathbf{0}_{b\times a} & \mathbf{0}_{b\times b} & \mathbf{0}_{b\times b} & \mathbf{I}_{b\times b} \end{bmatrix} \begin{Bmatrix} \ddot{\mathbf{u}} \\ \dot{\mathbf{u}} \\ \dot{\mathbf{V}} \\ \dot{\mathbf{J}} \\ \dot{\mathbf{V}}_\mathbf{c} \end{Bmatrix} + \begin{bmatrix} \mathbf{C_d} & \mathbf{K} & \mathbf{K}_{pzo} & \mathbf{0}_{a\times b} & \mathbf{0}_{a\times b} \\ -\mathbf{I}_{a\times a} & \mathbf{0}_{a\times a} & \mathbf{0}_{a\times b} & \mathbf{0}_{a\times b} & \mathbf{0}_{a\times b} \\ \mathbf{K}_{pzo}^T & \mathbf{0}_{b\times a} & \mathbf{0}_{b\times b} & -\mathbf{I}_{b\times b} & \mathbf{0}_{b\times b} \\ \mathbf{0}_{b\times a} & \mathbf{0}_{b\times a} & -\mathbf{L^{-1}} & -\mathbf{L^{-1}R} & \mathbf{L}^{-1} \\ \mathbf{0}_{b\times a} & \mathbf{0}_{b\times a} & \mathbf{0}_{b\times b} & -\mathbf{C^{-1}} & \mathbf{0}_{b\times b} \end{bmatrix} \begin{Bmatrix} \dot{\mathbf{u}} \\ \mathbf{u} \\ \mathbf{V} \\ \mathbf{J} \\ \mathbf{V_c} \end{Bmatrix} = \begin{Bmatrix} \mathbf{F} \\ \mathbf{0}_{a\times 1} \\ \mathbf{0}_{b\times 1} \\ \mathbf{0}_{b\times 1} \\ \mathbf{0}_{b\times 1} \end{Bmatrix} \tag{21}$$

where a and b are the number of free mechanical and electrical DOFs, respectively.

3.2. RL-Series Circuit

In abscence of external capacitive circuit impedance, equation (17) reduces to $V = RJ + L\dot{J}$, from which J is

$$J = R^{-1}V - R^{-1}L\dot{J} \tag{22}$$

Using equations (8), (19) and (22) and defining the state vector as $\{\dot{\mathbf{u}}, \mathbf{u}, \mathbf{V}, \mathbf{J}\}^T$, the SS matrices are arranged as follows,

$$\begin{bmatrix} \mathbf{M} & \mathbf{0}_{a\times a} & \mathbf{0}_{a\times b} & \mathbf{0}_{a\times b} \\ \mathbf{0}_{a\times a} & \mathbf{I}_{a\times a} & \mathbf{0}_{a\times b} & \mathbf{0}_{a\times b} \\ \mathbf{0}_{b\times a} & \mathbf{0}_{b\times a} & \mathbf{K}_{diel} & \mathbf{0}_{b\times b} \\ \mathbf{0}_{b\times a} & \mathbf{0}_{b\times a} & \mathbf{0}_{b\times b} & \mathbf{L} \end{bmatrix} \begin{Bmatrix} \ddot{\mathbf{u}} \\ \dot{\mathbf{u}} \\ \dot{\mathbf{V}} \\ \dot{\mathbf{J}} \end{Bmatrix} + \begin{bmatrix} \mathbf{C}_d & \mathbf{K} & \mathbf{K}_{piezo} & \mathbf{0}_{a\times b} \\ -\mathbf{I}_{a\times a} & \mathbf{0}_{a\times a} & \mathbf{0}_{a\times b} & \mathbf{0}_{a\times b} \\ \mathbf{K}_{piezo}^T & \mathbf{0}_{b\times a} & \mathbf{0}_{b\times b} & -\mathbf{I}_{b\times b} \\ \mathbf{0}_{b\times a} & \mathbf{0}_{b\times a} & -\mathbf{I}_{b\times b} & \mathbf{R} \end{bmatrix} \begin{Bmatrix} \dot{\mathbf{u}} \\ \mathbf{u} \\ \mathbf{V} \\ \mathbf{J} \end{Bmatrix} = \begin{Bmatrix} \mathbf{F} \\ \mathbf{0}_{a\times 1} \\ \mathbf{0}_{b\times 1} \\ \mathbf{0}_{b\times 1} \end{Bmatrix} \tag{23}$$

3.3. RL-Parallel Circuit

An RL parallel circuit connected to a piezoelectric source is depicted in figure 5, where C is the capacitance, L is the inductance and R is the electrical resistance. V_C, V_L and V_R are the voltage drops across them. J denotes the electric current.

An electrical circuit with a resistor and an inductor connected in parallel to a piezoelectric device is shown schematically in figure 5. L is the inductance, and R is the electrical resistance.

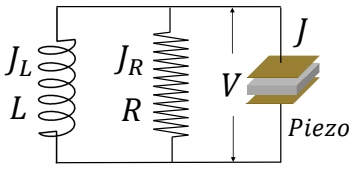

Figure 5. Scheme of piezoelectric device connected to a RL-Parallel circuit.

The voltage across the inductor is equal to that across the resistor. Using Ohm's law for the resistor and the inductor, this equality is expressed as

$$J_R R = L\frac{\partial J_L}{\partial t} \tag{24}$$

Naturally, both voltages are equal to that across the piezoelectric electrodes.

Introducing charge conservation law, $J = J_R + J_L$, in equation (24) gives

$$J_R R = L\left(\frac{\partial J_L}{\partial t} - \frac{\partial J_R}{\partial t}\right) \tag{25}$$

and finally,

$$V = L\frac{\partial J_L}{\partial t} - \frac{L}{R}\frac{\partial V}{\partial t} \tag{26}$$

Using equations (8), (19) and (26) and defining the state vector as $\{\dot{\mathbf{u}}, \mathbf{u}, \mathbf{V}, \mathbf{J_L}\}^T$, the SS matrices are arranged as follows,

$$\begin{bmatrix} \mathbf{M} & \mathbf{0}_{a\times a} & \mathbf{0}_{a\times b} & \mathbf{0}_{a\times b} \\ \mathbf{0}_{a\times a} & \mathbf{I}_{a\times a} & \mathbf{0}_{a\times b} & \mathbf{0}_{a\times b} \\ \mathbf{0}_{b\times a} & \mathbf{0}_{b\times a} & \mathbf{K}_{diel} & \mathbf{0}_{b\times b} \\ \mathbf{0}_{b\times a} & \mathbf{0}_{b\times a} & \mathbf{R}^{-1}\mathbf{L} & -\mathbf{L} \end{bmatrix} \begin{Bmatrix} \ddot{\mathbf{u}} \\ \dot{\mathbf{u}} \\ \dot{\mathbf{V}} \\ \dot{\mathbf{J}}_\mathbf{L} \end{Bmatrix} + \begin{bmatrix} \mathbf{C}_d & \mathbf{K} & \mathbf{K}_{piezo} & \mathbf{0}_{a\times b} \\ -\mathbf{I}_{a\times a} & \mathbf{0}_{a\times a} & \mathbf{0}_{a\times b} & \mathbf{0}_{a\times b} \\ \mathbf{K}_{piezo}^T & \mathbf{0}_{b\times a} & \mathbf{0}_{b\times b} & -\mathbf{I}_{b\times b} \\ \mathbf{0}_{b\times a} & \mathbf{0}_{b\times a} & \mathbf{I}_{b\times b} & \mathbf{0}_{b\times b} \end{bmatrix} \begin{Bmatrix} \dot{\mathbf{u}} \\ \mathbf{u} \\ \mathbf{V} \\ \mathbf{J_L} \end{Bmatrix} = \begin{Bmatrix} \mathbf{F} \\ \mathbf{0}_{a\times 1} \\ \mathbf{0}_{b\times 1} \\ \mathbf{0}_{b\times 1} \end{Bmatrix} \tag{27}$$

It should be noted that, in this case, the current in the state vector is the current flowing through the inductor J_L.

3.4. Pure Resistive R Circuit

If the circuit is purely resistive, SS equation can be reduced. In this case, the circuit equation reads

$$V = JR \tag{28}$$

Replacing equation (28) in equation (19), the following coupling equation is obtained,

$$\mathbf{K}_{piezo}^{T}\dot{\mathbf{u}} + \mathbf{K}_{diel}\dot{\mathbf{V}} - \mathbf{R}^{-1}\mathbf{V} = 0 \tag{29}$$

Using equations (8) and (29) and defining the state vector as $\{\dot{\mathbf{u}}, \mathbf{u}, \mathbf{V}\}^{T}$, the SS matrices are arranged as follows

$$\begin{bmatrix} \mathbf{M} & \mathbf{0}_{a\times a} & \mathbf{0}_{a\times b} \\ \mathbf{0}_{a\times a} & \mathbf{I}_{a\times a} & \mathbf{0}_{a\times b} \\ \mathbf{0}_{b\times a} & \mathbf{0}_{b\times a} & \mathbf{K}_{diel} \end{bmatrix} \begin{Bmatrix} \ddot{\mathbf{u}} \\ \dot{\mathbf{u}} \\ \dot{\mathbf{V}} \end{Bmatrix} + \begin{bmatrix} \mathbf{C}_d & \mathbf{K} & \mathbf{K}_{piezo} \\ -\mathbf{I}_{a\times a} & \mathbf{0}_{a\times a} & \mathbf{0}_{a\times b} \\ \mathbf{K}_{piezo}^{T} & \mathbf{0}_{b\times a} & -\mathbf{R}^{-1} \end{bmatrix} \begin{Bmatrix} \dot{\mathbf{u}} \\ \mathbf{u} \\ \mathbf{V} \end{Bmatrix} = \begin{Bmatrix} \mathbf{F} \\ \mathbf{0}_{a\times 1} \\ \mathbf{0}_{b\times 1} \end{Bmatrix} \tag{30}$$

As mentioned before, SS form (equation (14)) is obtained using elementary algebra, e.g., for RL-Series connection, matrices $\mathbf{A}$ and $\mathbf{B}$ are

$$[B] = \begin{bmatrix} \mathbf{M} & \mathbf{0}_{a\times a} & \mathbf{0}_{a\times b} & \mathbf{0}_{a\times b} \\ \mathbf{0}_{a\times a} & \mathbf{I}_{a\times a} & \mathbf{0}_{a\times b} & \mathbf{0}_{a\times b} \\ \mathbf{0}_{b\times a} & \mathbf{0}_{b\times a} & \mathbf{K}_{diel} & \mathbf{0}_{b\times b} \\ \mathbf{0}_{b\times a} & \mathbf{0}_{b\times a} & \mathbf{0}_{b\times b} & \mathbf{L} \end{bmatrix}^{-1} \tag{31}$$

and

$$[A] = -\begin{bmatrix} \mathbf{M} & \mathbf{0}_{a\times a} & \mathbf{0}_{a\times b} & \mathbf{0}_{a\times b} \\ \mathbf{0}_{a\times a} & \mathbf{I}_{a\times a} & \mathbf{0}_{a\times b} & \mathbf{0}_{a\times b} \\ \mathbf{0}_{b\times a} & \mathbf{0}_{b\times a} & \mathbf{K}_{diel} & \mathbf{0}_{b\times b} \\ \mathbf{0}_{b\times a} & \mathbf{0}_{b\times a} & \mathbf{0}_{b\times b} & \mathbf{L} \end{bmatrix}^{-1} \times \begin{bmatrix} \mathbf{C}_d & \mathbf{K} & \mathbf{K}_{piezo} & \mathbf{0}_{a\times b} \\ -\mathbf{I}_{a\times a} & \mathbf{0}_{a\times a} & \mathbf{0}_{a\times b} & \mathbf{0}_{a\times b} \\ \mathbf{K}_{piezo}^{T} & \mathbf{0}_{b\times a} & \mathbf{0}_{b\times b} & -\mathbf{I}_{b\times b} \\ \mathbf{0}_{b\times a} & \mathbf{0}_{b\times a} & -\mathbf{I}_{b\times b} & \mathbf{R} \end{bmatrix} \tag{32}$$

4. System analysis

4.1. Modal characterisctics

The Laplace transform of SS equation (14) allows obtaining the transformed state vector,

$$X(s) = (s\,[\mathbf{I}] - [\mathbf{A}])^{-1}\,[\mathbf{B}]\,X(s) \tag{33}$$

where s is the complex Laplace variable or complex frequency. The Laplace transform of the system output is calculated acording to

$$Y(s) = [\mathbf{D}_1]\,X(s) \tag{34}$$

from equation (33) and equation (34),

$$Y(s) = [\mathbf{D}_1]\,(s\,[\mathbf{I}] - [\mathbf{A}])^{-1}\,[\mathbf{B}]\,X(s) \tag{35}$$

Using matrix adjoint and determinant quotiem to calculate $(s\,[\mathbf{I}] - [\mathbf{A}])^{-1}$, the input-output transfer function $H_{yx}(s)$ is obtained from 35

$$H_{yx}(s) = [\mathbf{D}_1] \left(\frac{adj(s\,[\mathbf{I}] - [\mathbf{A}])}{\det(s\,[\mathbf{I}] - [\mathbf{A}])} \right) [\mathbf{B}] \tag{36}$$

The characteristic equation of the system results,

$$\det(s\,[\mathbf{I}] - [\mathbf{A}]) = 0 \tag{37}$$

The system poles are values of s satisfying equation (37). System poles possess information on the damping factor and the damped frequency of each mode of the system. Computing the real and imaginary parts of the eigenvalues, the damping factor introduced in each mode by the presence of a dissipative circuit could be determined. If all but electrical resistance parameters are fixed, the root locus $s(R)$ will show the poles and zeros movement in the complex plane. Each complex root has the form $\lambda = -\zeta\omega_n \pm \omega_n\sqrt{(\zeta^2 - 1)}$. If $\zeta \leq 0$, there are two conjugated complex roots and natural frequency and damping are calculated as

$$\omega_n = \|\lambda\| \tag{38}$$

$$\zeta = -\frac{Real(\lambda)}{\omega_n} \tag{39}$$

4.2. Steady state frequency response

If the structure is loaded with a harmonic signal $q(t) = q_0 e^{(j\omega t)}$, after the transient, the system response is represented by the state vector,

$$x(t) = \mathbf{H}_{xq} q_0 e^{(j\omega t)} \tag{40}$$

Transfer matrix $\mathbf{H}_{xq}$ relates the system state vector with the input q_0 in stationary state. The time derivative of the state vector is

$$\dot{x}(t) = j\omega \mathbf{H}_{xq} q_0 e^{(j\omega t)} \tag{41}$$

After the transient response,

$$j\omega \mathbf{H}_{xq} U e^{(j\omega t)} = \mathbf{A}\mathbf{H}_{xq} q_0 e^{(j\omega t)} + \mathbf{B} q_0 e^{(j\omega t)} \tag{42}$$

The transfer function finally is

$$\mathbf{H}_{xq} = (j\omega t\mathbf{I} - \mathbf{A})^{-1}\mathbf{B} \tag{43}$$

The output is simply calculated by multipling equation (43) by $\mathbf{D}1$

$$\mathbf{H}_{yq} = \mathbf{D}_1 \mathbf{H}_{xq} \tag{44}$$

4.3. Transient response

The linear system SS is a first order model whose total response for initial state $x(0) = X_0$ can be calculated as

$$x(t) = e^{\mathbf{A}t}x(0) + \int_0^t e^{\mathbf{A}(t-\tau)}\mathbf{B}q(\tau)d\tau \tag{45}$$

where the first term of the right hand side is the zero-input response, while the term containing the integral gives the zero-state response. The output can be calculated as follows

$$y(t) = \mathbf{D}_1\left[e^{\mathbf{A}t}x(0) + \int_0^t e^{\mathbf{A}(t-\tau)}\mathbf{B}q(\tau)d\tau\right] + \mathbf{B}q(t) \tag{46}$$

4.4. Electrical Power Output

Instantaneous electrical power dissipated in a resistor of value R is calculated as

$$p(t) = \frac{v(t)^2}{R} \tag{47}$$

where $v(t)$ is the instantaneous voltage drop in the resistor. The mean power over a time window of length T is

$$P_{mean} = \frac{1}{T}\int_0^T \frac{v^2(t)}{R}dt \tag{48}$$

In a steady state frequency response analysis, the mean electrical power over a period $T = \frac{2\pi}{\omega}$ is calculated as follows,

$$P_{mean} = \frac{V_0^2}{2R} = \frac{V_{rms}^2}{R} \tag{49}$$

where V_0 is the modulus of te harmonic voltage drop and V_{rms} is the square root of the mean squared voltage drop over period T calculated acording to

$$V_{rms} = \sqrt{\frac{1}{T}\int_0^T \left[v(t)\right]^2 dt} = \frac{V_0}{\sqrt{2}} \tag{50}$$

In this paper, the instantaneous voltage drop for transient analysis is obtained by identifying the corresponding entry in the state vector $\{x\}$. Besides, for steady-state frequency response analysis,

$$V_0 = \sum_{j=1}^{n_x} H_{xq}(i,j)q(\omega)(j) \tag{51}$$

where n_x is the number of system states and $H_{xq}(i,j)$ is the entry of transfer matrix H_{xq} relating voltage drop identiefied with index i and the input signal in enrtry j of $q(\omega)$.

5. Piezoelectromechanical Modelling Package (PEMPack)

To conduct the numerical experiments presented in this paper, a whole modelling and simulation package named **PEMPack** was designed and implemented by the authors in GNU/Octave V5.0.2 [26]. PEMPack binds an FE module, an electrical circuit module, a system solver module and a post-processing toolset. The developed package allows building the model, running different analyses and post-processing results, representing a useful tool to study the influence of the electrical impedance on system response, damping, natural frequencies and electrical power output. **PEMPack** contains the following modules:

- Piezoelectric shell FE [23]
- FE model assembly
- Boundary conditions and load application
- Electrical network builder and coupling
- Partitioning and rearrangement of system matrices and vectors
- FE to SS translator
- Frequency response, modal and transient analysis

Based on the SS form of the electromechanical system, valuable calculations, namely root locus, transient dynamic response and steady-state frequency response, are easily afforded. In this way, a complete picture of system characteristics and performance can be obtained. The developed package takes advantage of the standard linear algebra numerical engine already implemented in GNU/Octave and could be used as a tool for the design of micro EH systems.

The developed PEMPack package can deal with different impedances (RLC) ranging from pure resistive, inductive and capacitive to any combination of them. Moreover, series and parallel combinations are allowed. The developed package sets the corresponding equations in a systematic/automatic manner.

6. Comparison between numerical results and experimental measurements

In this section, the EH system experimentally tested in [27] is numerical analysed and normalized electrical power and voltage obtained are compared with esperimental results. The EH system consists of a cantilever aluminium beam with a bonded piezoelectric composite patch. Figure 6 shows the experiment layout, dimensions and the FE mesh.

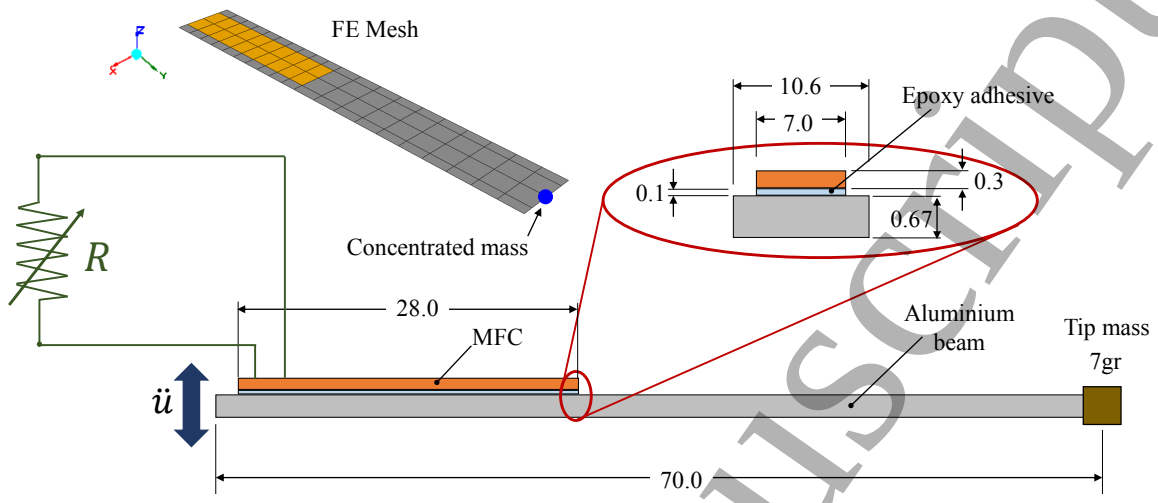

Figure 6. Cantilever beam experimentally tested in [27]. Lengths are in $[mm]$

Material properties are summarised in table 1. Element size ranges between 1.8 and $4.5mm$.

Properties	
	MFC 2807-P2
Trans. Isot. Mech. elastic	
E_p (GPa)	15.857
E_t (GPa)	30.336
ν_p	135.8
ν_{tp}	88.3
G_{tp} (GPa)	90.42
Piezoelectric $e_{13}(C/m^2)$	5.16
Dielectric (F/m)	2.34E-8
Mass Density (Kg/m^3)	5440.0
	Aluminium
Isotropic elastic	
Elastic modulus (GPa)	68.9
Poisson's ratio	0.33
Mass density (kg/m^3)	2700
	Epoxy
Isotropic elastic	
Elastic modulus (GPa)	2.7
Poisson's ratio	0.4
Mass density (kg/m^3)	1100

Table 1. Material properties used for the numerial analysis of the EH beam experimentally tested in [27].

A mechanical damping ratio of 2.0% of critical [25] is used in all modes.

MFC used in [27] is a P2-type device, i.e. its polling direction is through the thickness; thus, a proper conversion is needed so that the numerical results using the proposed shell FE with UFAEF can be directly compared to experimental results. Assuming that the mechanical stress induced by the electric field and that the voltage V between electrodes are the same in both cases [29], the following relation holds,

$$e_{13}\frac{V}{t_h} = e_{11}\frac{V}{\delta_e} \tag{52}$$

where e_{13} and t_h are the actual P2-type MFC electromechanical coupling and thickness, respectivelly. e_{11} and δ_e are the model MFC coupling along fibre and interdigitated electrode fingers spacing, respectivelly. If the value of e_{13} in the experiment is used for e_{11} in the model, the equivalent electrode spacing in the model δ_e should be equal to the MFC P2-type thickness $t_h = 0.3[mm]$.

Following [27], a frequency response analysis is performed at two excitation frequencies, 30.0 and 135.0 [Hz]. The normalized electrical power plots for both situations are shown in figure 7, where experimental results presented in [27] are also included for comparison. Normalized electrical power at each resistance value R is calculated as the ratio between the mean power corresponding to that R and the peak power over all the considered resistance range.

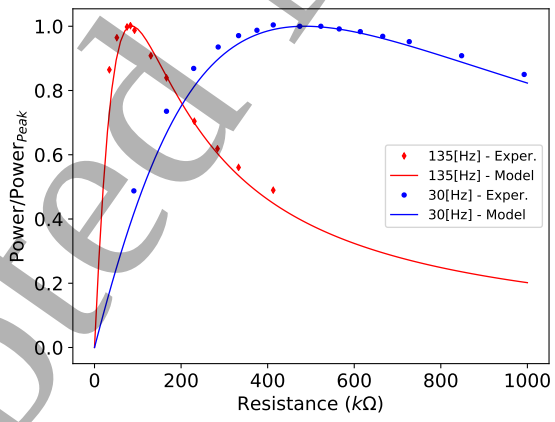

Figure 7. Variation of normalized power output with electrical resistance. Numerical and experimental results comparison.

A good agreement between experimental measurements and numerical results obtained using the developed tools is observed. The value of electrical resistance for the maximum output electrical power is also obtained. The numerically estimated optimal resistance value is 430 [kΩ] presenting a 5% difference with respect to that reported in [27], $R = 410$ [kΩ]. Differences between numerical and experimental normalized power are within 10%. Finally, the output voltage variation with excitation frequency is plotted in figure 8.

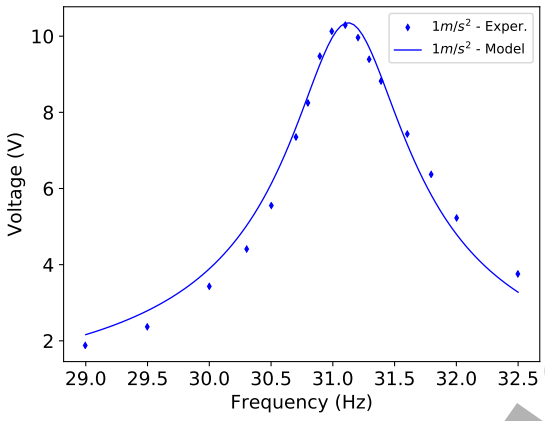

Figure 8. Variation of output voltage with frequency. Numerical and experimental results comparison

Figure 8 shows that differences between numerical results and experimental measurements are within 7.0% in the frequency band ranging from 30.0 to 32.0 [Hz]; outside this band differences increase but they are always lower than 30.0%

7. Application example

The structural system analysed is a cantilever, PVC foam-cored, aluminium closed-box beam whose cross-section shape corresponds to a NACA 0010 symmetric aerodynamic profile. The structure is depicted in figure 9.

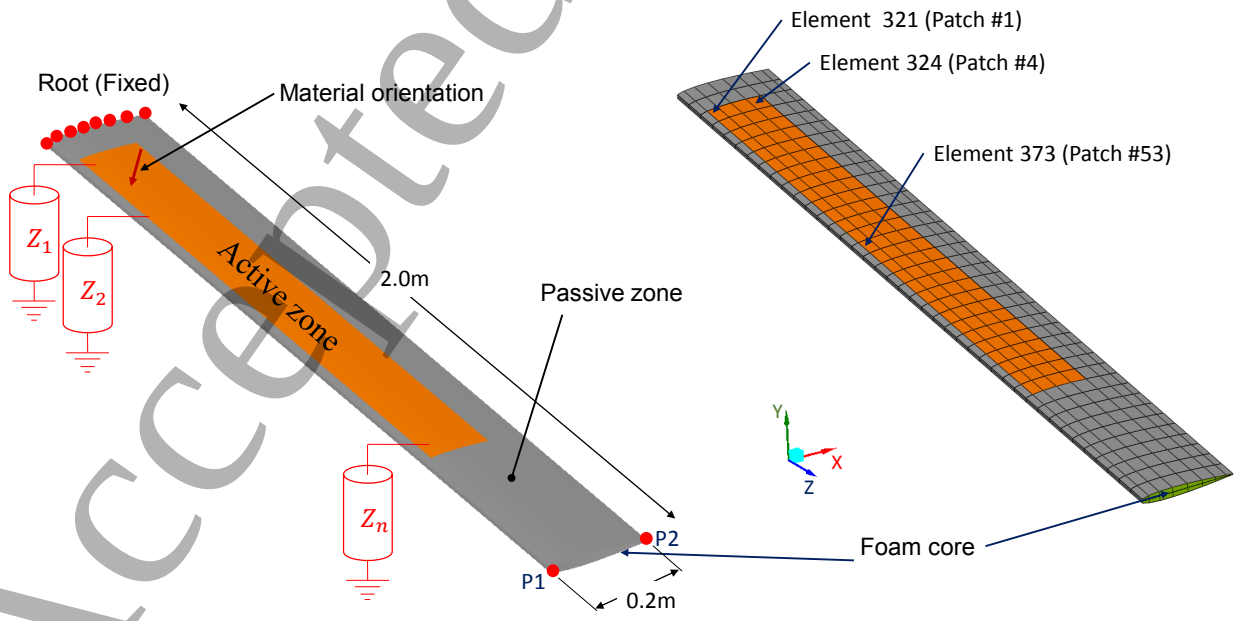

Figure 9. Closed-box cantiliever beam with piezoelectric devices.

On the upper and lower surfaces, active devices made of PCPIE material are bonded to the passive aluminium skin. Each piezoelectric patch poses two electric terminals connected to internal electrodes. One terminal of each patch is grounded while the other is connected to the external network.

The PCPIE properties are estimated as described in [30], particularized for the linear electromechanical behaviour. Pure PZT-5H material, as well as obtained composite electromechanical linear properties, are listed in table 2. Aluminium and epoxy material properties are summarized in table 3. Linear elastic material properties from [31] are used for the foam and they are also presented in table 3.

Properties	PZT-5H	PCPIE
Mech. elastic (GPa)		
C_{11}	130.6	26.4
C_{12}	85.66	13.0
C_{22}	135.8	52.5
C_{31}	88.3	7.2
C_{32}	90.42	12.1
C_{33}	121.3	24.3
C_{44}	23.47	14.0
C_{55}	22.9	8.6
C_{66}	22.9	13.1
Piezoelectric (Cm^2)		
e_{14}	17.03	2.36
e_{21}	-6.9	-0.7
e_{22}	22.9	16.9
e_{23}	7.07	-0.7
e_{36}	17.06	1.9
Dielectric (Fm^{-1})		
χ_{11}	1.27E-8	6.1E-9
χ_{22}	1.27E-8	8.3E-9
χ_{33}	1.51E-8	5.6E-9
Density (Kg/m^3)	7500.0	4500.0

Table 2. Pure PZT-5H and PCPIE material properties.

Properties	Aluminium	PVC Foam	EPOXY
Elastic modulus (E, GPa)	71.0	0.077	4.7
Poisson ratio (ν)	0.33	0.32	0.3
Density (ρ, Kg/m^3)	2713.0	80.0	2100.0

Table 3. Isotropic material properties.

Generalized proportional damping [28] is used in all numerical computations. For the analyses performed, a mechanical damping ratio of 2.0% of critical [25] is used in all modes.

The model mesh is presented in figure 9 where restrained nodes, applied force locations and electric ports for EH computations are identified. Element size ranges between 10 and 40 [mm].

Displacements are restrained at the beam-box root. Two mechanical loading cases are considered for each of the analysis in both frequency and time domain. For frequency response analysis, one load case consists of a bending moment (concentrated 0.5 [N] forces applied at P1 and P2, see figure 9) while the second load case is a torsional couple (concentrated 6.43 [N] forces applied at P1 and P2 in opposite directions). For time response analysis, only a torsional couple of magnitude 2.0 [Nm] (concentrated 10.0 [N] forces applied at P1 and P2 in opposite directions) is used and two unitary temporal signals are considered; on the one hand, a harmonic signal of frequency 109.7 [Hz], on the other hand, a rectangular pulse of 0.02 [s] duration time.

8. Results

Three electrical network cases, namely, pure resistive, RL-Series and RL-Parallel, are considered to be connected to the piezoelectric active zones of the structural system. In each case, the coupled system is analysed and the results are presented in this section.

8.1. Pure Resistive Circuit. Modal analysis and frequency response.

Modal analysis for both open-circuit and short-circuit conditions, and frequency response analysis are performed for a range of electrical resistance. The variation of modal frequency and damping with the electrical resistance for the first eight modes is presented in figure 10. From second-order system theory, the eigenvalues of matrix **A** are, in general terms, complex numbers containing modal frequency and damping information. For the case of underdamped systems, the damping and frequency are calculated using equations (38) and (39). Since circuit impedance affects entries of the matrix **A**, modal properties are affected by resistance and inductance matrix. This aspect is reflected in figure 10, where a change in modal frequency is observed for certain resistance value. Maximum modal damping is observed in correspondence with the frequency change.

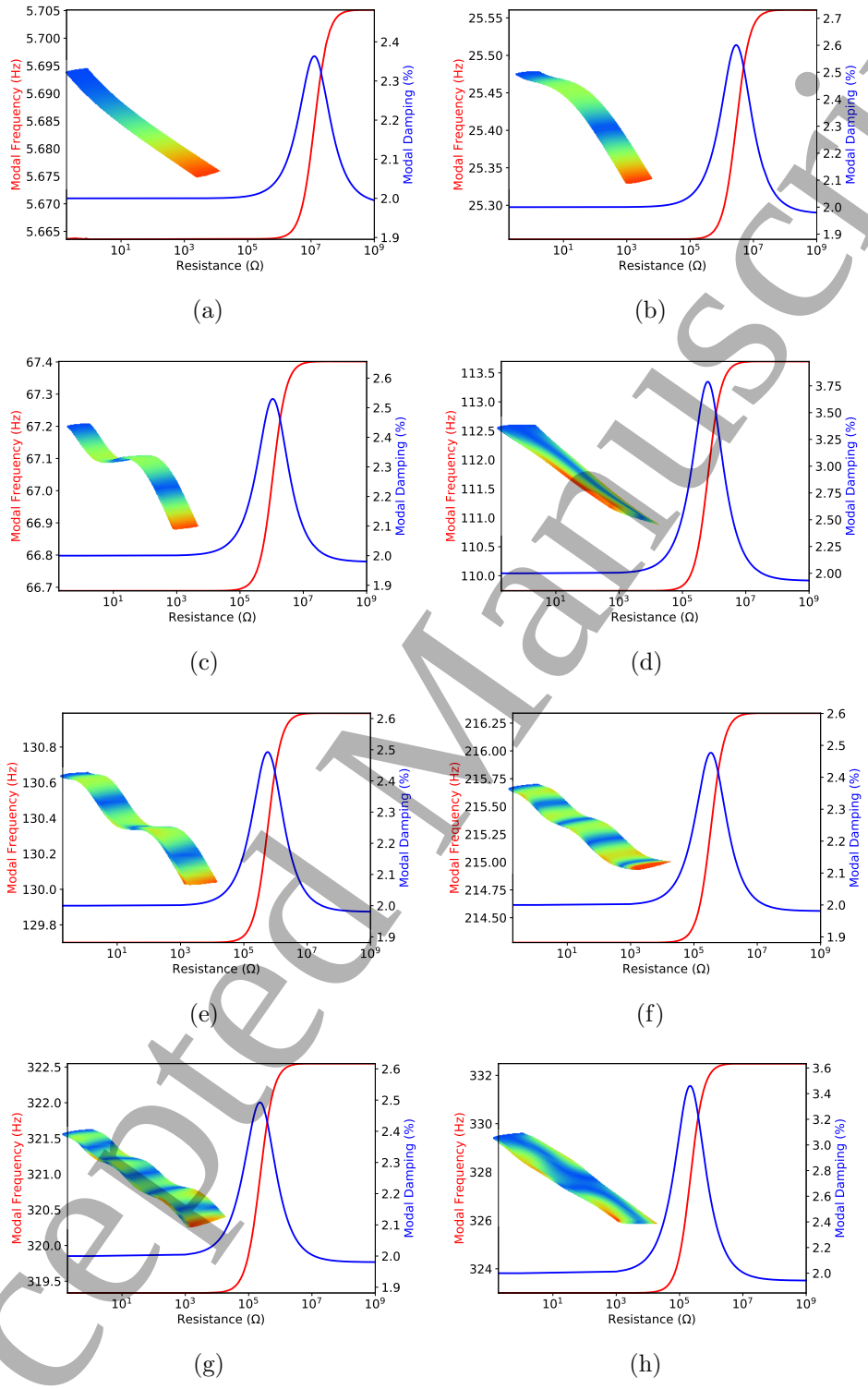

Figure 10. Modal properties. (a)Mode shape #1, flexural; (b)Mode shape #2, flexural; (c)Mode shape #3, flexural; (d)Mode shape #4, torsional; (e)Mode shape #5, flexural; (f)Mode shape #6, flexural; (g)Mode shape #7, flexural; (h)Mode shape #8, torsional

The modal analysis of the coupled system with variable load resistance connected

reveals essential characteristics. If the resistance is gradually increased, it is observed that during a certain range of resistance values, the damping remains unchanged until particular resistance value is reached. If the resistance value increases over this value, an increase in the damping ratio is observed until a maximum value is reached. From this point, if the resistance is further increased, the damping starts to decrease until the base value is retrieved.

The modal frequency is observed to increase during the interval in which damping goes from structural (base) damping to its maximum value and then, turns back to the base value. This frequency switch remains after the maximum damping point. Further increase of the resistance does not produce more increment in modal frequency. The modal frequency change observed between open and short-circuit conditions can be explained based on the finite element equation (12). For open-circuit condition, a matrix formed as a triple product of the electromechanical and the dielectric matrices is added to the mechanical stiffness matrix. Hence, at open-circuit conditions, the structure stiffens and natural frequencies increase.

Besides, the gradual change of natural frequencies and damping between open and short-circuit conditions can be explained in terms of the eigenvalues of the characteristic equation 37), since they are gradually affected by resistance values variations. The damping factor introduced in each mode by the presence of the dissipative circuit is determined by computing the real and imaginary parts of the eigenvalues of the characteristic equation.

Modal parameters evaluation shows the existence of resistance values for which the damping is maximum. Computational tools to determine optimal resistance values can be successfully used to tune-up energy harvesting systems. According to [32], the structural, electromechanical coupling can be quantified using the approximate expression,

$$K^2 = \frac{(f_{oc}^2 - f_{sc}^2)}{f_{sc}^2} \tag{53}$$

where f_{oc} is the open-circuit or anti-resonance frequency, i.e. corresponding to $R \to \infty$ and f_{sc} is the short-circuit or resonance frequency i.e. $R \to 0$. Natural frequencies, coupling factors, maximum damping and electrical resistance for maximum damping for the first ten modes are detailed in table 4. Letters F and T in the first column stand for flexural and torsional mode, respectively.

Mode	f_{sc} [Hz]	f_{oc} [Hz]	K^2	Max. Total Damping	Max. Electric Damping	$R[M\Omega]$ @Max. Damp.
1 (F)	5.67	5.71	1.47	2.364	0.364	12.98
2 (F)	25.26	25.56	2.44	2.601	0.601	2.900
3 (F)	66.69	67.40	2.15	2.530	0.530	1.100
4 (T)	109.74	113.7	7.34	3.790	1.790	0.6680
5 (F)	128.70	130.99	2.00	2.493	0.493	0.5780
6 (F)	214.28	216.34	1.93	2.477	0.477	0.3440
7 (F)	319.33	332.55	2.03	2.493	0.493	0.2360
8 (T)	323.00	332.48	5.96	3.460	1.460	0.2180
9 (F)	448.57	452.85	1.92	2.473	0.473	0.1690
10 (T)	526.82	938.89	4.63	3.140	2.140	0.1350

Table 4. Coupling factors, damping and optimal resistances.

In consistency with the coupling factor values detailed in table 4, the fourth natural frequency is considerably affected by the electrical resistance and this fact is also evidenced in figure 10(d). The frequency change is produced for resistance values between $1.0E5$ and $1.0E6$ [Ω] while maximum damping is obtained for $6.68E5$ [Ω].

Figure 11 shows plots of modal damping vs resistance varying from short-circuit to open-circuit condition for the first ten modes.

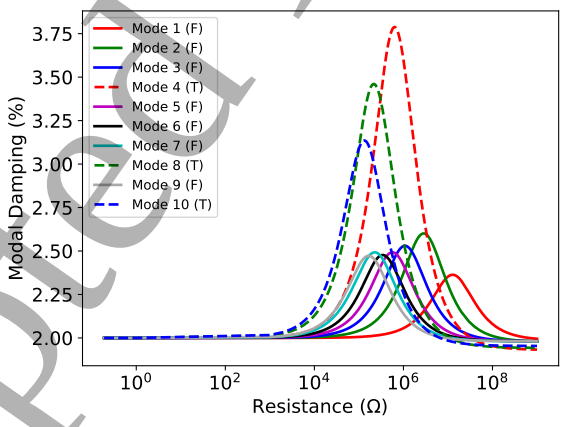

Figure 11. Modal damping vs. resistance.

Figure 11 shows that each mode has an optimal resistance value for which maximum damping is obtained. The maximum modal damping occurs for the fourth mode (torsional mode) at a resistance value of $6.68E5$ [Ω].

A frequency response analysis is considered and the normalized vertical displacement of point P1 for a harmonic tip torque is calculated and presented in figure 12. Normalized displacement is calculated as the ratio between the displacement at each frequency and the displacement at the lowest frequency (quasi-static response). A set

of curves is obtained for three resistances representing open-circuit, short-circuit and intermediate values for which maximum damping is observed for mode #4.

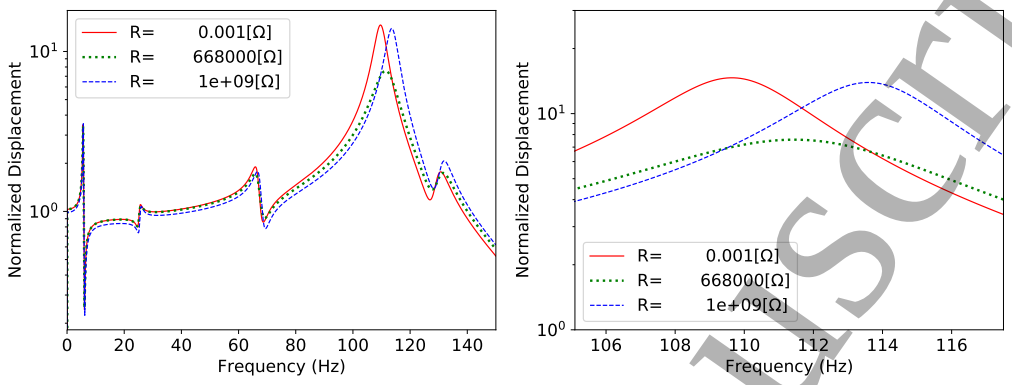

Figure 12. Frequency response. (a) Entire analysed range. (b)Response in the vecinity of the fourth natural frequency.

Figure 12 reflects high amplifications values corresponding to both open-circuit ($R = 1.0E9$ [Ω]) and short-circuit ($R = 0.001$ [Ω]) conditions, while for $R = 6.68E5$ [Ω] a flat response is obtained at resonance frequency. Figures 12(b) shows in more detail the response in the vecinity of the fourth natural frequency.

Figures 13(a) and 13(b) present the power generated in piezoelectric patch #4 for resistance values ranging from short-circuit ($R \to 0.0$) to open-circuit ($R \to \infty$). Harmonic, torsional and flexural excitation, are respectively used as input. Excitation frequencies in correspondence to the first five natural modes of the structure are considered.

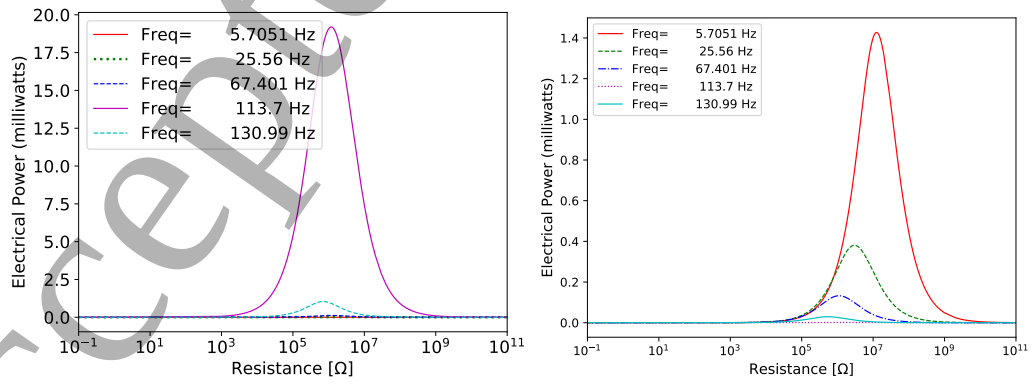

Figure 13. Electrical power generated in patch #4. (a) Torsional excitation; (b) Flexural excitation.

Figures 13(a) and 13(b) reflect the influence of the electrical resistance values on

the power generated in piezoelectric zones of the structure. The power depends not only on the resistance value but on the excitation mode as well. Maximum power is delivered for resistance value $R = 668$ [kΩ], when a torsional harmonic excitation of 113.7 [Hz] is applied.

8.2. RL-Serial. Harmonic mechanical excitation

The electrical network considered for the preceding model includes only electrical resistances. The following example considers resistive-inductive impedances connected in series. The resistance value is $R = 5.0E4$ [Ω] while three values of inductance are considered. The mechanical excitation is a tip torque of magnitude 2.0 [Nm] modulated by a harmonic signal of 109.7 [Hz] frequency.

The displacement time history response corresponding to point P1 is depicted in figure 14 .

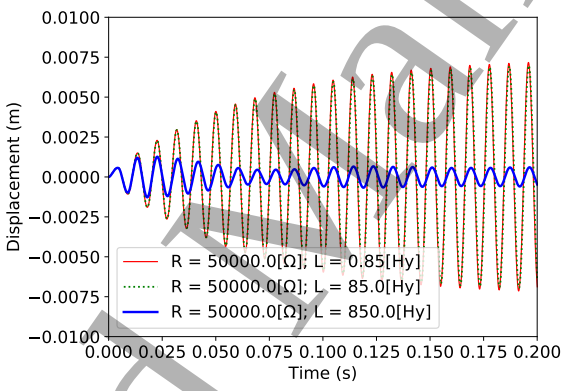

Figure 14. Displacement history - RL Series. Harmonic excitation.

Almost the same displacements are obtained for $L = 0.85$ [Hy] and $L = 85.0$ [Hy] while for $L = 850.0$ [Hy], a 10% of those values is registered.

The electric voltage and electric current arising in patch #1 is presented in figures 15, 16 and 17 for the three inductive impedances considered.

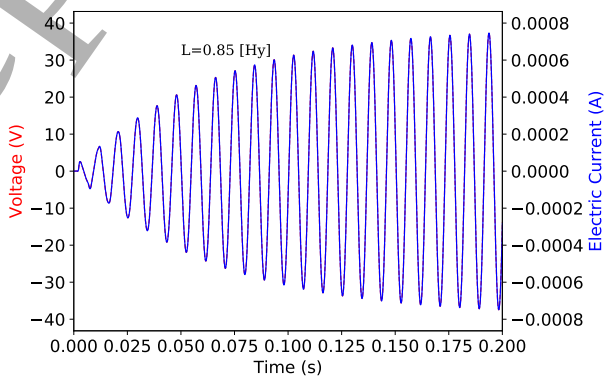

Figure 15. Electric potential and current history - RL Series. Inductance: 0.85 [Hy]. Harmonic excitation.

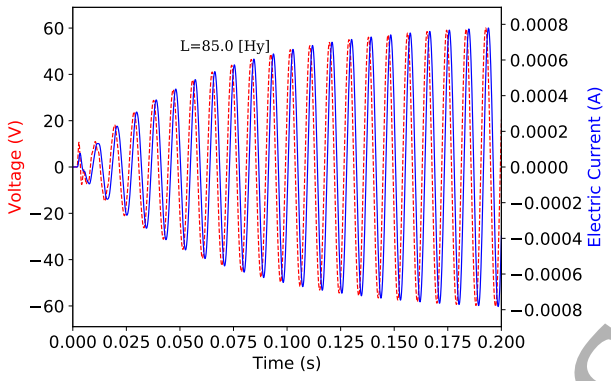

Figure 16. Electric potential and current history - RL Series. Inductance: 85.0 [Hy]. Harmonic excitation.

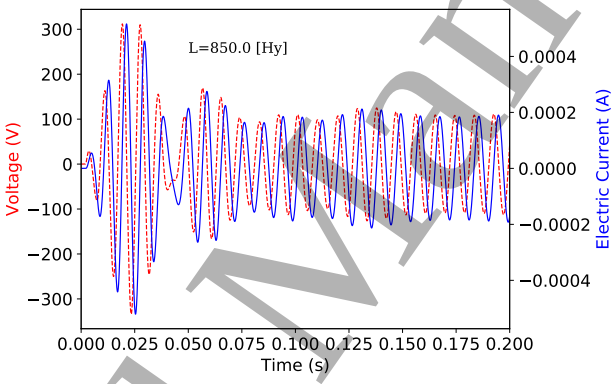

Figure 17. Electric potential and current history - RL Series. Inductance: 850.0 [Hy]. Harmonic excitation.

The electrical power output on patch #1 when the structure is excited by a tip torque modulated by a rectangular pulse signal is also calculated and presented in figure 18 for the three RL-Serial impedances considered,

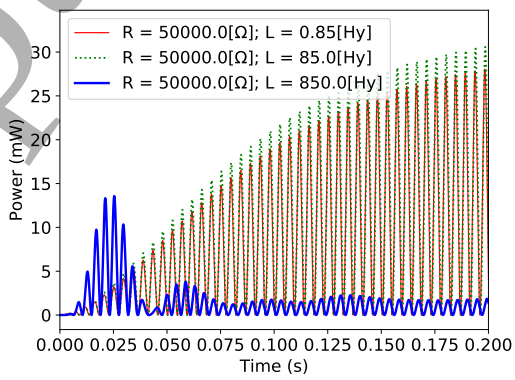

Figure 18. Electrical power history - RL Series. Harmonic excitation.

Figure 18 shows that the long term maximum electrical power harvested with RL-Series circuit occurs for inductance $L = 85.0$ [Hy]. This is consistent with voltages

(V) and electric currents (J) depicted in figures 15, 16, 17. For $L = 850.0$ [Hy] the substantially lower power level obtained is due to both the low electric current and the lag between electric current and voltage as well. On the other hand, for $L = 0.85$ [Hy], in spite that J is of the same order as for $L = 85.0$ [Hy] case, the lag between electric current and voltage makes output power slightly less than for $L = 85.0$ [Hy] case. It is observed that within the first 0.05 [s], the maximum power output is registered for $L = 850.0$ [Hy]. This fact is consistent with the corresponding electric current and voltage signals plotted in figure 17.

8.3. RL-Serial. Rectangular pulse mechanical excitation

The same three RL-Serial impedances used in section 8.2 are considered in this example. The mechanical excitation corresponds to a tip torque of magnitude 2.0 [Nm] modulated by a rectangular pulse signal of 0.02 [s] duration time. The displacement time history response corresponding to point P1 is depicted in figure 19.

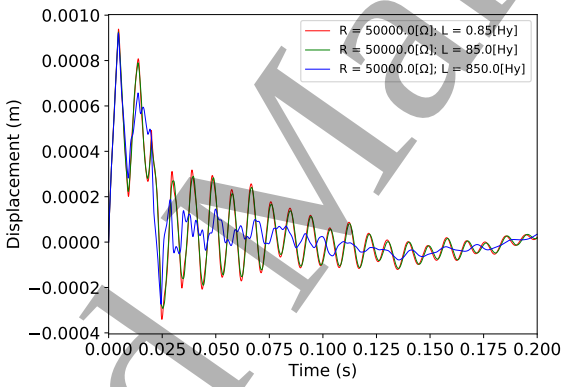

Figure 19. Displacement history - RL Series. Rectangular pulse excitation.

The electric voltage and the electric current arising in patch #1 are presented in figures 20, 21 and 22 for the three inductive RL-Serial impedances considered.

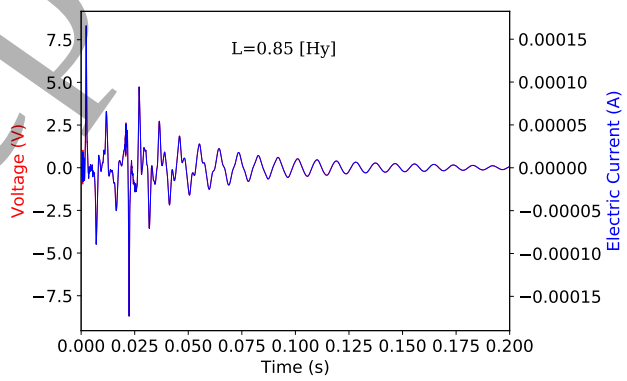

Figure 20. Electric potential and current history - RL Series. Inductance: 0.85 [Hy]. Rectangular pulse excitation.

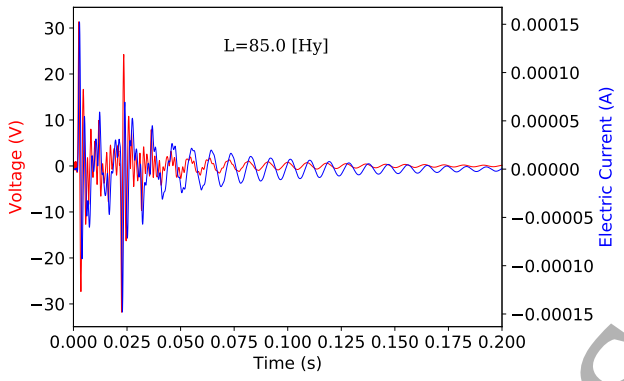

Figure 21. Electric potential and current history - RL Series. Inductance: 85.0 [Hy]. Rectangular pulse excitation.

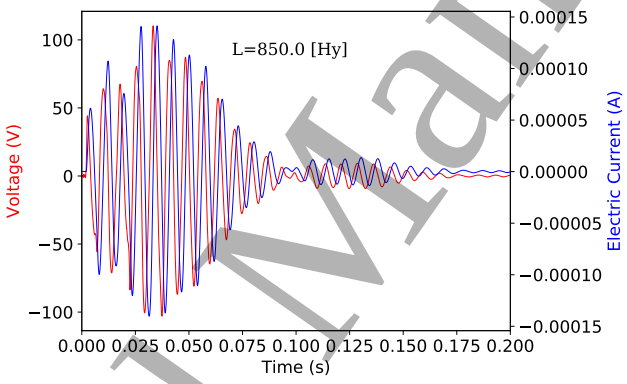

Figure 22. Electric potential and current history - RL Series. Inductance: 850.0 [Hy]. Rectangular pulse excitation.

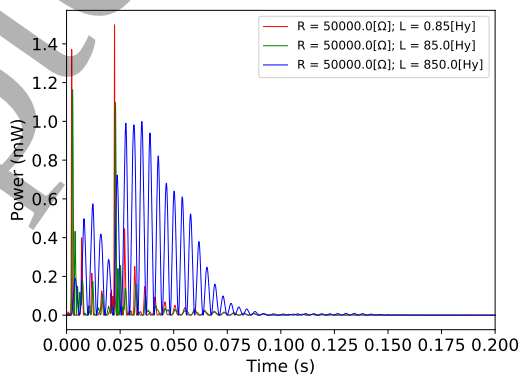

Figure 23. Electrical power history - RL Series. Rectangular pulse excitation.

Figure 23 shows that the maximum instantaneous electrical power harvested with RL-Series circuit occurs for inductance $L = 0.85$ [Hy] with narrow peaks, while with $L = 850.0$ [Hy] slightly lower but wider peaks of power are supplied. This is consistent

with voltages (V) and electric currents (J) depicted in figures 20 and 22. The low power level obtained with $L = 85.0$ [Hy] is explained by the lag between voltages (V) and electric current (J) depicted in figure 21.

8.4. RL-Parallel. Harmonic mechanical excitation

The following example considers resistive-inductive impedances connected in parallel. A constant resistance value $R = 5.0E4$ [Ω] is used while three values of inductive impedance are considered. A tip torque of magnitude 2.0 [Nm] modulated by a harmonic signal is applied and the electrical power supplied from patch #1 for the three inductive impedances considered is calculated and presented in figure 25,

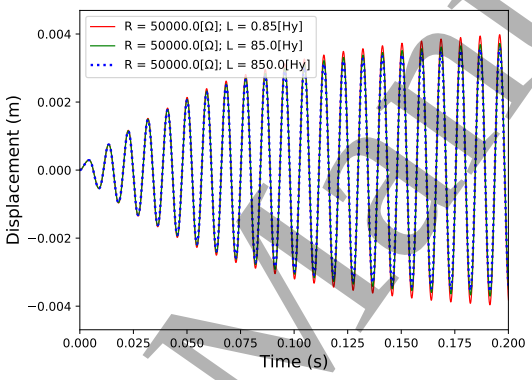

Figure 24. Displacement history - RL Parallel. Harmonic excitation.

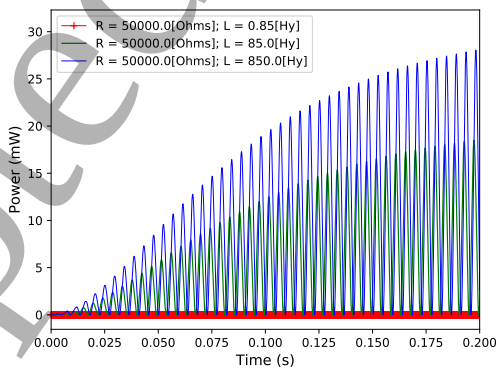

Figure 25. Electrical power history - RL Parallel. Harmonic excitation.

The maximum electrical power harvested with RL-parallel circuit is obtained when inductance value is $L = 850.0$ [Hy] as shown in figure 25.

8.5. RL-Parallel. Rectangular pulse mechanical excitation

In this example, the mechanical excitation is modulated by a rectangular pulse signal. The electrical power output on patch #1 is calculated for three inductances while a

constant resistance value $R = 5.0E4$ [Ω] is used. Electrical power curves are presented in figure 27,

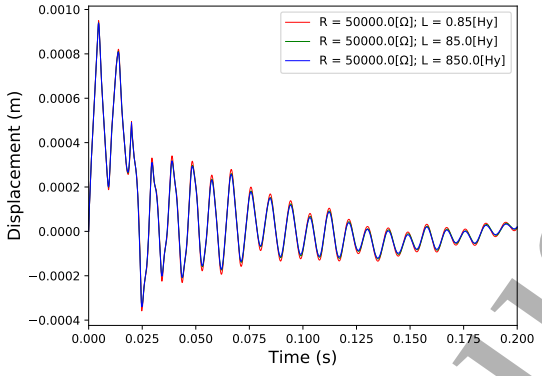

Figure 26. Displacement history - RL Parallel. Rectangular pulse excitation.

The influence of the inductance value on damping produced by the electrical resistance is captured by the numerical models. Comparing figures 14 and 24 on the one hand, and figures 19 and 26 on the other hand, it is observed that maximum damping is produced for 850.0 [Hy] inductance value.

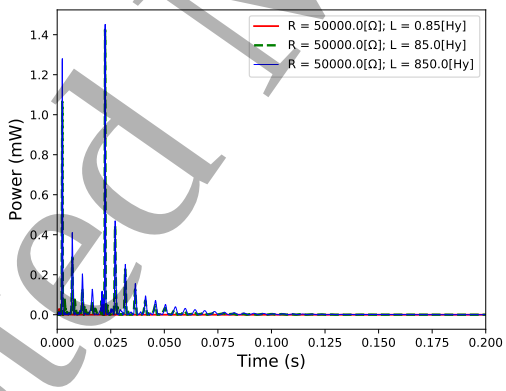

Figure 27. Electrical power history - RL Parallel. Rectangular pulse excitation.

The maximum electrical power harvested with RL-parallel circuit is obtained when inductance value is $L = 850.0$ [Hy] as shown in figure 27.

Comparing figures 23 and 27, it is observed that for RL-Series and rectangular pulse excitation, maximum instantaneous electrical power harvested occurs for inductance $L = 0.85$ [Hy] with narrow peaks, while with $L = 850.0$ [Hy] slightly lower but scattered peaks of power are delivered. For RL-Parallel and harmonic excitation, maximum output power occurs for $L = 850.0$ [Hy].

Table 5 summarizes the inductance values for maximum power estimated using time history computations for the different cases considered.

Circuit	Excitation	L[Hy] at which Max. power is obtained	L[Hy] for scattered power peaks
RL-Serial.	Harmonic	85.0	-
RL-Serial.	Rect. pulse	0.85	850.0
RL-Parallel	Harmonic	850.0	-
RL-Parallel	Rect. pulse	850.0	85.0 and 850.0

Table 5. Impedances for maximum output power.

9. Conclusions

A numerical tool developed with the aim of analysing micro energy harvesting systems, based on piezoelectric composites polarised with interdigitated electrodes, is presented in this paper. The numerical tool comprises the implementation of a piezoelectric shell FE using the UFAEF concept and a program to manage the FE model, transform it in SS model, include the electrical network equations, solve the coupled system and finally post-process the raw results.

Two micro-electric generation plants equipped with piezoelectric devices are numerically evaluated. Firstly, as a model validation step, a cantilever beam for which experimental test results are available from the open literature is analysed; numerical and experimental values of output power and voltage are in good agreement, maximum differences are less than 10%.

Secondly, a closed box beam with piezoelectric devices bonded to its skin is modelled. The energy generated when it is externally excited by harmonic and transient forces, as well as the damping introduced in the structure are computed. The model successfully captures the dependence of modal frequency and damping on circuit resistance. For torsional modes, the peak modal damping as well as the resistance value at which this peak value is obtained decreases with the increase of mode frequency. The same behaviour is observed for all computed flexural modes, except for the first flexural mode for which the resistance value causing maximum modal damping is considerably higher than the resistance value producing the maximum damping in the rest of them. The frequency response analysis performed allows to determine resistance values producing maximum damping.

The influence of the mechanical excitation mode is assessed showing that, due to the piezoelectric fibres orientation, torsional modes have higher electromechanical coupling factors than flexural modes. Output power is computed for both excitation modes. For torsional excitation, power level is found to be up to 15 times higher than that for flexural excitation.

Based on a time history response analysis, the inductance influence on power output is analysed. For RL circuits with fixed resistance value and harmonic tip torque excitation, the maximum electrical power harvested is observed to depend on

the inductance value and the circuit layout. For series circuit connection, maximum power occurs for low inductance values, while for parallel connection, maximum power is registered at higher inductance value.

When rectangular pulse excitation is used, narrow peaks pattern is observed for low impedance values, while scattered peaks of power are delivered when the high impedance is connected. The same behaviour is observed in both series and parallel connection layouts.

Acknowledgments

The financial support of CONICET and the Research Council of National University of Tucumán (CIUNT) is gratefully acknowledged. The authors also wish to thank Amelia Campos for her collaboration in the English revision.

References

[1] Xinlin Qing, Wenzhuo Li, Yi-Shou Wang, and Hu Sun. Piezoelectric transducer-based structural health monitoring for aircraft applications. *Sensors*, 19:545, 01 2019.

[2] Heung Soo Kim, Joo-Hyong Kim, and Jaehwan Kim. A review of piezoelectric energy harvesting based on vibration. *Int J Pr Eng Man*, 12(6):129–1141, 2011.

[3] M. I. Tiwana, S. J. Redmond, and N.H. Lovell. A review of tactile sensing technologies with applications in biomedical engineering. *Sensor Actuat A-Phys*, 179(C):17–31, 2012.

[4] Xuexian Chen, Yu Song, Zongming Su, Haotian Chen, Xiaoliang Cheng, Jinxin Zhang, Mengdi Han, and Haixia Zhang. Flexible fiber-based hybrid nanogenerator for biomechanical energy harvesting and physiological monitoring. *Nano Energy*, 5 2017.

[5] A.C Turkmen and C. Celik. Energy harvesting with the piezoelectric material integrated shoe. *Energy*, 2018.

[6] K.S. Ramadan, D. Sameoto, and S. Evoy. A review of piezoelectric polymers as functional materials for electromechanical transducers. *Smart Mater Struct*, 23(3):033001, 2014.

[7] Niell Elvin and Alper Erturk. *Advances in Energy Harvesting Methods*. 2013.

[8] M. Karimi, A.H. Karimi, R. Tikani, and S. Ziaei-Rad. Experimental and theoretical investigations on piezoelectric-based energy harvesting from bridge vibrations under travelling vehicles. *International Journal of Mechanical Sciences*, 119, 2016.

[9] F. Khamendeifar and S. Arzanpour. Energy harvesting from pnuematic tires using piezoelectric transducers. In *ASME Conference on Smart Materials, Adaptive Structures and Intelligent Systems*, 2008.

[10] G. Manla, N. M. White, and J. Tudor. Harvesting energy from vehicle wheels. In *TRANSDUCERS*, pages 1389–1392, 2009.

[11] P.F Musgrave, W. Zhou, and L. Zuo. Piezoelectric energy harvesting from torsional vibration. In *ASME Vol.8: 27th Conf. on Mech. Vibr. and Noise*, 2015.

[12] A. Toprak and O. Tigli. Piezoelectric energy harvesting: State-of-the-art and challenges. *Applied Physics Reviews*, 1:031104,1–14, 2014.

[13] N.W. Hagood and Von Flotow. A damping of structural vibrations with piezoelectric materials and passive electrical networks. *J Sound Vib*, 146:243–268, 1991.

[14] S. Koshigoe and J.W. Murdock. A unified analysis of both active and passive damping for a plate with piezoelectric transducers. *J Acoust Soc Am*, 93(5):346–584, 1993.

[15] D. Saravanos. Damped vibration of composite plates with passive piezoelectric-resistor elements. *J Sound Vib*, 22(5):867–885, 1999.

[16] G. A. Lesieutre, G. K. Ottman, and H. F. Hofmann. Damping as a result of piezoelectric energy harvesting. *J Sound Vib*, 269:991–1001, 2004.

[17] Ugur Aridogan, Ipek Basdogan, and Alper Erturk. Random vibration energy harvesting on thin plates using multiple piezopatches. *J Intell Mater Syst Struct*, 27(20):2744–2756, 2016.

[18] Tian-Bing Xu, Emilie J Siochi, Jin Ho Kang, Lei Zuo, Wanlu Zhou, Xiudong Tang, and Xiaoning Jiang. Energy harvesting using a PZT ceramic multilayer stack. *Smart Mater Struct*, 22(6):065015, 2013.

[19] A. Benjeddou. Advances in piezoelectric finite element modeling of adaptive structural elements: a survey. *Computer and Structures*, 76:347 – 363, 2000.

[20] Adnan Harb. Energy harvesting: State-of-the-art. *Renewable Energy*, 36(10):2641 – 2654, 2011.

[21] Xinlei Fu and Wei-Hsin Liao. Nondimensional model and parametric studies of impact piezoelectric energy harvesting with dissipation. *J Sound Vib*, 429:78 – 95, 2018.

[22] Yang Kuang and Meiling Zhu. Evaluation and validation of equivalent properties of macro fibre composites for piezoelectric transducer modelling. *Compos Part B-Eng*, 158:189 – 197, 2019.

[23] A.E. Guennam and B.M. Luccioni. Piezoelectric shell FE for the static and dynamic analysis of piezoelectric fibre composite laminates. *Smart Mater Struct*, 18:095044 (12pp), 2009.

[24] E. L. Pradeesh and S. Udhayakumar. Investigation on the geometry of beams for piezoelectric energy harvester. *Microsystem Technologies*, 2018.

[25] S. Paquin and Y. St-Amant. Improving the performance of a piezoelectric energy harvester using a variable thickness beam. *Smart Materials and Structures*, 19(10):105020, 2010.

[26] J.W Eaton, D. Bateman, S. Hauberg, and R. Wehbring. *GNU Octave version 5.2.0 manual: a high-level interactive language for numerical computations*, 2020.

[27] D. Upadrashta and Y. Yang. Experimental investigation of performance reliability of macro fiber composite for piezoelectric energy harvesting applications. *Sensors and Actuators A: Physical*, 244:223 – 232, 2016.

[28] R.W Clough and J. Penzien. *Dynamics of Structures*. Computers and Structures, Inc., 2003.

[29] Y. Yang, L. Tang, and H. Li. Vibration energy harvesting using macro-fiber composites. *Smart Mater Struct*, 18:031104, 2009.

[30] A.E. Guennam and B.M. Luccioni. Model for piezoelectric/ferroelectric composites polarized with interdigitated electrodes. *Compos Struct*, 131:312–324, 2015.

[31] Gilmer M. Viana and Leif A. Carlsson. Mechanical properties and fracture characterization of cross-linked pvc foams. *J. of Sandw Struct Mater*, 4(2):99–113, 2002.

[32] R. Lerch. Simulation of piezoelectric devices by two- and three-dimensional finite elements. *IEEE Transactions on Ultrasonics, Ferroelectrics, and Frequency Control*, 37(3):233–247, 1990.